

# Heavy flavour production at HERA

Uri Karshon

Weizmann Institute of Science, Rehovot, Israel  
On behalf of the H1 and ZEUS Collaborations

E-mail: [uri.karshon@weizmann.ac.il](mailto:uri.karshon@weizmann.ac.il)

**Abstract.** The copious production of charm quarks at HERA has yielded a detailed understanding of QCD dynamics, the only measure of the charm contribution to the proton structure, as well as measurements of the charm mass and the fragmentation parameters of charmed hadrons. Although with smaller samples, measurements of beauty production also place constraints on the structure of the proton and allow a measurement of the beauty quark mass. Several measurements of heavy quark production using different decay modes, are presented, both new individual measurements from the H1 and ZEUS Collaborations, as well as combined data. These provide a powerful vindication of the form of the gluon density in the proton derived from scaling violations of inclusive deep inelastic scattering data. QCD fits to the data lead to measurements of the charm and beauty masses and also provide precise predictions for e.g. W and Z production at the LHC. Additionally, fragmentation fractions to the ground state charm hadrons are compared to  $e^+e^-$  data and previous HERA results. The data have a precision similar to that of the  $e^+e^-$  data and support the hypothesis that fragmentation is independent of the production process.

## 1. Introduction

Production of the ground-state charm mesons  $D$  and  $D^*$  was extensively studied at the HERA  $ep$  collider. Since the photon coupling to a charm quark is stronger than that to the down-quarks (d,s,b), the charm production cross section is large. Two kinematic regimes exist at HERA: Photoproduction (PHP) with  $Q^2 \approx 0$  where the scattered electron is undetected and Deep Inelastic Scattering (DIS) with  $Q^2 > \text{few GeV}^2$  where the scattered electron is detected. Here  $Q^2$  is the exchanged photon virtuality. The charm contribution to inclusive DIS cross section at HERA is up to 30%. The dominant process for heavy quark production (charm,  $c$ , or beauty,  $b$ ) in DIS is boson-gluon fusion, where a gluon from the proton interacts with the photon, W or Z from the incoming electron. Thus, this process is a direct probe of the gluon density in the proton. It is also sensitive to the masses of these heavy quarks,  $m_Q$ , and enables testing QCD by comparing data to next-to-leading order (NLO) predictions. Multiple scales in this process ( $Q^2$ ,  $m_Q$  and transverse momentum of the heavy quark) allow perturbative calculations. The  $c$  and  $b$  contributions to the proton structure function,  $F_2$ , can be extracted. Fractions of charm quarks hadronising to charm hadrons can test the universality of the fragmentation fractions.

The HERA  $ep$  collider operated with electrons or positrons at 27.5 GeV and protons at 820 or 920 GeV. About  $126 \text{ pb}^{-1}$  of data were taken between 1995 - 2000 (“HERA I”) and  $\approx 373 \text{ pb}^{-1}$  were taken between 2003 - 2007 (“HERA II”) by each of the two main general experiments H1 and ZEUS.

## 2. Theory of heavy quark production

Several NLO schemes for heavy quark production in  $ep$  collisions exist:

1) “Massive” or Fixed Flavour Number Scheme (FFNS), where  $Q^2 \approx m_Q^2$ . In this scheme only three active flavours (u,d,s) in the proton are considered, the  $c$  or  $b$  quark is produced only perturbatively in the hard scattering and mass effects are correctly included.

2) “Massless” or Zero-Mass Variable Flavour Number Scheme (ZM-VFNS), where  $Q^2 \gg m_Q^2$ . Here the  $c$  or  $b$  quark is treated as a massless parton, its density is added as a fourth flavour in the proton and a resummation of large logarithms of  $Q^2/m_Q^2$  is performed.

At intermediate  $Q^2$  both schemes should be merged:

3) General-Mass Variable Flavour Number Scheme (GM-VFNS). This scheme is equivalent to FFNS for  $Q^2 \approx m_Q^2$  and to ZM-VFNS for  $Q^2 \gg m_Q^2$ . In between, various schemes interpolate differently from each other. In this scheme, the heavy-quark mass is treated as an effective mass parameter,  $M_Q$ , of the various interpolation models.

The double differential cross section  $\frac{d^2\sigma^{Q\bar{Q}}}{dx dQ^2}$  can be expressed as:  $\frac{2\pi\alpha^2}{xQ^4} [(1 + (1 - y)^2)F_2^{Q\bar{Q}} - y^2 F_L^{Q\bar{Q}}]$ , where  $x$  is the Bjorken variable,  $y = Q^2/(sx)$  is the fraction of the incoming electron momentum carried by the exchanged photon,  $s$  is the total energy squared of the  $ep$  system and  $F_2^{Q\bar{Q}}$ ,  $F_L^{Q\bar{Q}}$  are the heavy-quark contributions to the proton structure functions  $F_2$  and  $F_L$ .

A reduced heavy-quark cross section,  $\sigma_{red}^{Q\bar{Q}}$ , can be defined as:  $\frac{d^2\sigma^{Q\bar{Q}}}{dx dQ^2} = \frac{2\pi\alpha^2}{xQ^4} [(1 + (1 - y)^2)\sigma_{red}^{Q\bar{Q}}]$ .

## 3. $D^{*\pm}$ photoproduction at three centre-of-mass energies

$D^{*\pm}$  mesons were selected by the ZEUS Collaboration using the decay channel  $D^{*\pm} \rightarrow D^0\pi_s^\pm$  with the subsequent decay  $D^0 \rightarrow K^-\pi^+$ , where  $\pi_s$  refers to a low-momentum (“slow”) pion accompanying the  $D^0$ [1]. Hereafter charge-conjugate states are included.

In Figs.1-3 the distributions of  $M(K^-\pi^+\pi_s^+) - M(K^-\pi^+)$  are shown at three centre-of-mass (CM) energies: HER, MER, LER ( $\sqrt{s} = 318, 251, 225$  GeV) in the kinematic region  $1.9 < p_T^{D^*} < 20$  GeV,  $|\eta^{D^*}| < 1.6$ ,  $Q^2 < 1$  GeV<sup>2</sup>,  $0.167 < y < 0.802$ , where  $p_T^{D^*}$  is the  $D^*$  transverse momentum and  $\eta^{D^*}$  is the  $D^*$  pseudorapidity.

Clear  $D^{*\pm}$  signals are seen. Backgrounds are estimated by fitting simultaneously correct- and wrong-sign,  $M(K^-\pi^-\pi_s^+) - M(K^-\pi^-)$ , distributions in the range  $\Delta M < 0.168$  GeV.

Visible  $D^*$  PHP cross sections are obtained from  $\sigma_{vis}(D^*) = \frac{N^{data}(D^*)}{A \cdot BR \cdot \mathcal{L}}$ , where  $BR = B(D^* \rightarrow D^0\pi) \cdot B(D^0 \rightarrow K\pi) = 0.0263$ ,  $A$  is the acceptance and  $\mathcal{L}$  is the integrated luminosity.

In Figure 4 the ratio of the visible cross sections to the highest energy one,  $R_\sigma = \frac{\sigma_i}{\sigma_{HER}}$ ;  $i = HER, MER, LER$ , is shown. Higher precision of the energy dependence of the cross sections is obtained in the ratio since some systematic uncertainties in data and theory cancel. The data are compared to FFNS NLO predictions. The cross sections increase with increasing  $ep$  CM energy, as predicted by NLO QCD.

## 4. Charm fragmentation fractions in photoproduction

The production of  $D^0, D^{*+}, D^+, D_s^+$  and  $\Lambda_c$  charm hadrons has been studied by ZEUS[2]. The data were used to measure the fragmentation fractions of  $c$ -quarks hadronising into these charm hadrons defined as:  $f(c \rightarrow charm\ hadron) = \sigma(charm\ hadron)/\sigma(total\ charm\ production)$ . The measurements were performed in the PHP regime:  $Q^2 < 1$  GeV<sup>2</sup>. The charm hadrons were reconstructed in the kinematic range:  $p_T > 3.8$  GeV,  $|\eta| < 1.6$ ,  $130 < W < 300$  GeV, where  $W$  is the  $\gamma p$  CM energy. The charm hadrons were measured in the decay modes:  $D^0 \rightarrow K^-\pi^+$ ,  $D^+ \rightarrow K^-\pi^+\pi^+$ ,  $D^{*+} \rightarrow D^0\pi_s^+ \rightarrow K^-\pi^+\pi_s^+$ ,  $D_s^+ \rightarrow \phi\pi^+$ ,  $\Lambda_c^+ \rightarrow K^-\pi\pi^+$ . The total charm production cross section is given by:  $\sigma_{tot} = \sigma(D^0) + \sigma(D^+) + \sigma(D_s^+) + 1.14\sigma(\Lambda_c^+)$ , where the rates of the charm-strange baryons relative to the  $\Lambda_c^+$  was estimated from the non-charm sector to be about 14%.

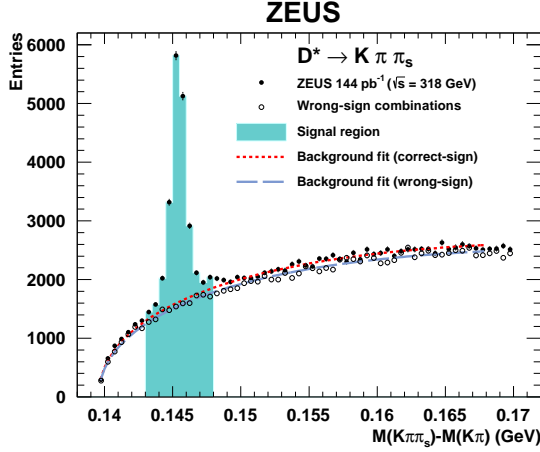


**Figure 1.** Distributions of  $M(K\pi\pi_s) - M(K\pi)$  for the HER data sample: Correct-sign (wrong-sign) combinations are filled circles (empty circles). Background fit is short-dashed (long-dashed) line for correct-(wrong-)sign combinations.

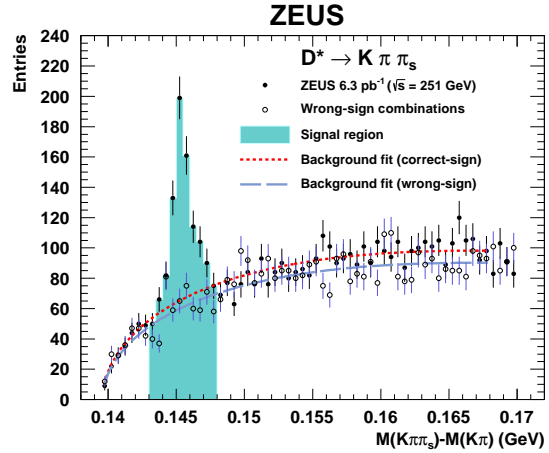


**Figure 2.** Distributions of  $M(K\pi\pi_s) - M(K\pi)$  for the MER data sample. Other details as in Fig.1.

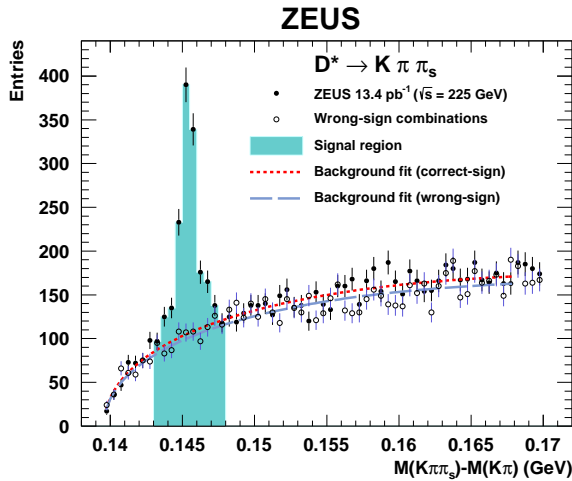


**Figure 3.** Distributions of  $M(K\pi\pi_s) - M(K\pi)$  for the LER data sample. Other details as in Fig.1.

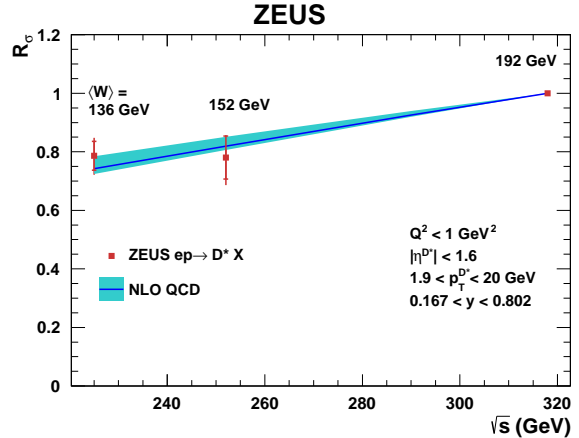


**Figure 4.** Normalised  $D^*$  visible PHP cross sections as a function of the  $ep$  CM energy. Data (points) are shown with statistical uncertainties (inner error bars) and statistical and systematic uncertainties (outer error bars). NLO QCD predictions (solid line) are shown with uncertainties (band). At each data point, the average  $\gamma p$  CM energy,  $\langle W \rangle$ , is given.

Clear charm hadron signals are seen for all channels (not shown). The charm fragmentation fractions are shown in Figure 5 (left column) with comparisons to previous results. The precision is competitive with the combined  $e^+e^-$  results (right column). The fragmentation fractions are found to be independent within errors of the production mechanism, supporting the hypothesis of universality of heavy-quark fragmentation. This universality is supported also by new LHC pp data by the ALICE and LHCb Collaborations.

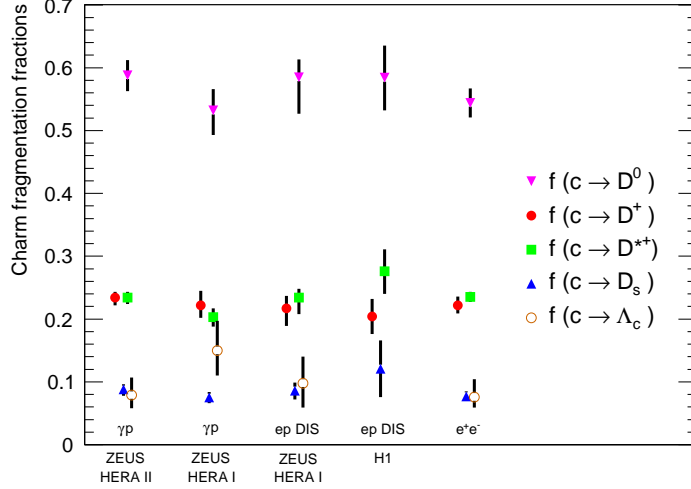


**Figure 5.** Fragmentation fractions of  $c$ -quarks hadronising to the charm hadrons  $D^0$ ,  $D^{*+}$ ,  $D^+$ ,  $D_s^+$  and  $\Lambda_c$  in PHP (left column) compared to previous results.

### 5. $D^\pm$ production in DIS

$D^\pm$  production has been studied by ZEUS in DIS with the full HERA II data[3]. A clean signal of  $8356 \pm 198$   $D^+$  events in the  $M(K^-\pi^+\pi^+)$  distribution is seen (not shown). In Figs.6-9  $D^+$  differential cross sections are given w.r.t.  $Q^2, y, p_T(D^+), \eta(D^+)$  in the kinematic region  $5 < Q^2 < 1000$   $\text{GeV}^2$ ,  $1.5 < p_T(D^+) < 15$   $\text{GeV}$ ,  $|\eta(D^+)| < 1.6$ ,  $0.02 < y < 0.7$ , where  $p_T(D^+)$  and  $\eta(D^+)$  are, respectively, the  $D^+$  transverse momentum and pseudorapidity. NLO predictions based on FFNS describe the data well.

The differential cross section  $d\sigma/dy$  for different  $Q^2$  bins was used to extract  $F_2^{c\bar{c}}$  at reference points  $x_i, Q_i^2$  for each bin  $i$  using  $F_{2,meas}^{c\bar{c}}(x_i, Q_i^2) = \sigma_{i,meas} \frac{F_{2,theo}^{c\bar{c}}(x_i, Q_i^2)}{\sigma_{i,theo}}$ . Here  $F_{2,theo}$  and  $\sigma_{i,theo}$  are calculated at NLO in FFNS with the HVQDIS program.

The results are shown in Figure 10 and compared to predictions of GM-VFNS and FFNS. The NLO calculations describe the new precise data well.

### 6. HERA charm data combination in DIS

Nine data sets of  $D^*, D^+, D^0, \mu$  and lifetime tags with 155 H1 and ZEUS cross section measurements from various HERA I and HERA II analyses were combined[4].

In Figure 11 the reduced cross section is shown as a function of  $x$  at a fixed  $Q^2$  value of 18  $\text{GeV}^2$  in the kinematic range  $2.5 < Q^2 < 2000$   $\text{GeV}^2$ ;  $3 \cdot 10^{-5} < x < 5 \cdot 10^{-2}$ . Correlated systematics for the combined result (filled circles) are fully taken into account. The uncertainty of the combined result is about a factor 2 better than each of the most precise data sets.

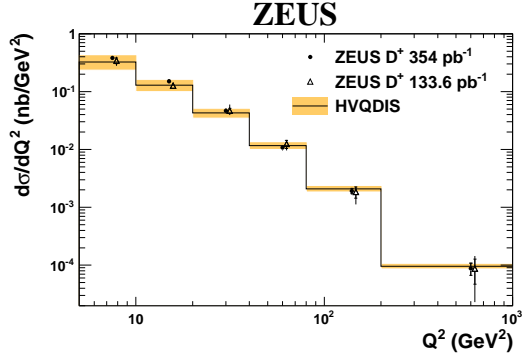


**Figure 6.**  $D^+$  differential cross section as a function of  $Q^2$ . Solid line and shaded band are NLO FFNS predictions.

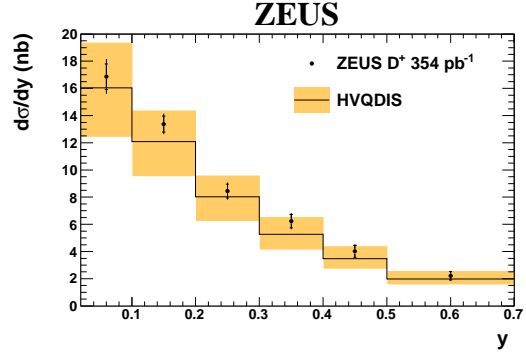


**Figure 7.**  $D^+$  differential cross section as a function of  $y$ . Solid line and shaded band are as in Figure 6.

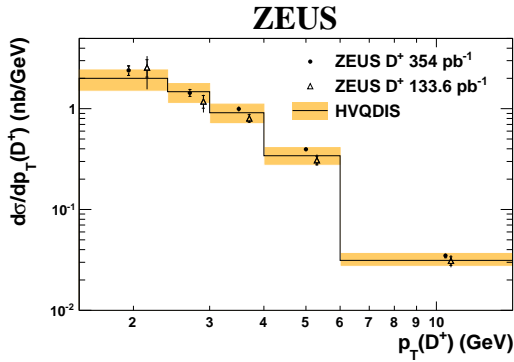


**Figure 8.**  $D^+$  differential cross section as a function of  $p_T(D^+)$ . Solid line and shaded band are as in Figure 6.

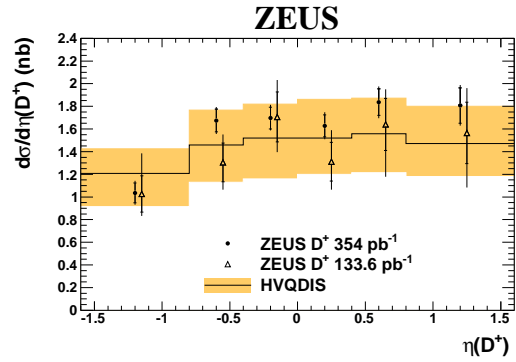


**Figure 9.**  $D^+$  differential cross section as a function of  $\eta(D^+)$ . Solid line and shaded band are as in Figure 6.

In Figure 12 the combined  $\sigma_{red}^{c\bar{c}}$  as a function of  $x$  for fixed  $Q^2$  values is compared to the mixed massive-massless scheme GM-VFNS predictions in the RT standard scheme. The lines are predictions with  $M_c = 1.4$  GeV. The large theory uncertainties are dominated by the  $M_c$  variation. Within the uncertainties, the GM-VFNS scheme describes the data well.

A combined NLO analysis has been performed in the kinematic range  $W > 15$  GeV,  $x < 0.65$  and  $Q^2 > 3.5$  GeV<sup>2</sup> using  $\sigma_{red}^{c\bar{c}}$  together with the combined inclusive DIS cross sections. For each heavy flavour (HFL) scheme, parton density function (PDF) fits were performed with  $1.2 < M_c < 1.8$  GeV. The  $\chi^2$  values of these fits for the various schemes as a function of  $M_c$  are shown in Figure 13. The minimal  $\chi^2$  values for each scheme (stars), called  $M_c^{opt}$ , are observed at different values of  $M_c$ . In Figure 14,  $\sigma_{red}^{c\bar{c}}$  as a function of  $x$  is shown for  $Q^2 = 5$  and 7 GeV<sup>2</sup> and compared to the fit results of the various VFNS schemes. The upper plots are for  $M_c = 1.4$  GeV and the lower plots are for  $M_c = M_c^{opt}$ . The data are described much better with  $M_c = M_c^{opt}$  than with fixed  $M_c$  and the predictions of all schemes with  $M_c^{opt}$  are very similar to each other.

The PDFs obtained from fits to the HERA data by the  $M_c$  scanning procedure in the different VFNS schemes are used to calculate cross section predictions for  $W^\pm$  and  $Z^0$  production at the LHC at  $\sqrt{s} = 7$  TeV. The predicted  $W^+$  and  $Z^0$  cross sections are shown in Figs.15-16 for

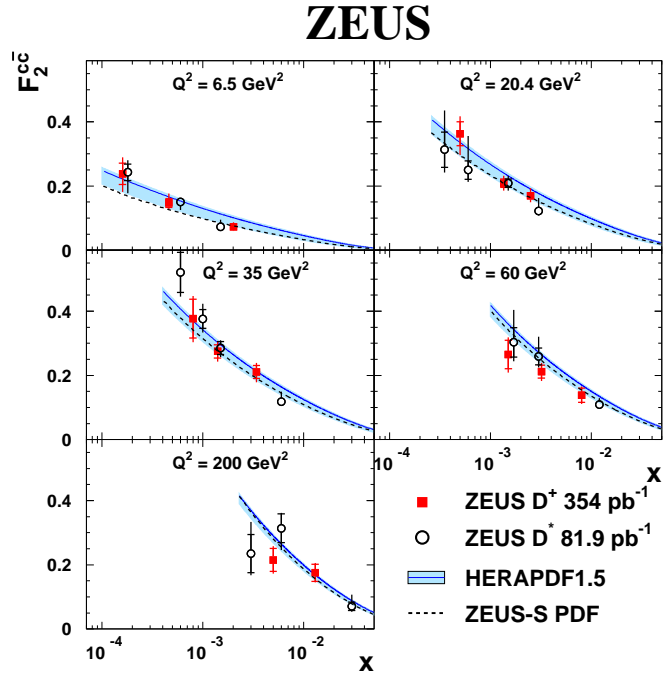


**Figure 10.** Structure function  $F_2^{c\bar{c}}$  as a function of  $x$  for various  $Q^2$  values compared to GM-VFNS (“HERAPDF1.5”) and FFNS (“ZEUS-S PDF”) predictions.

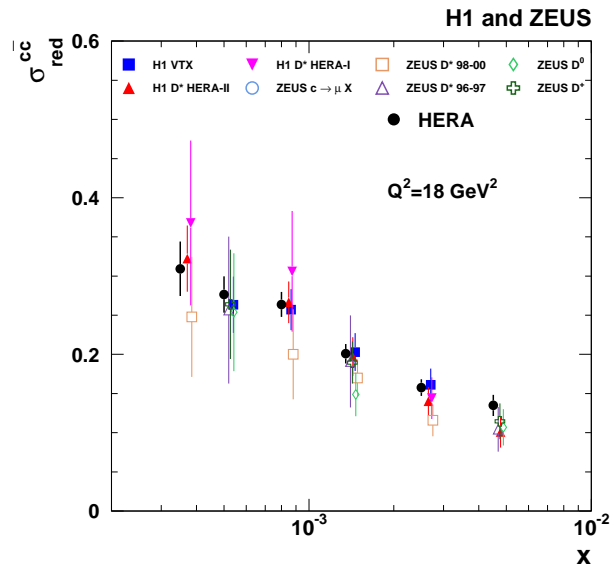


**Figure 11.** Combined reduced cross sections  $\sigma_{red}^{c\bar{c}}$  as a function of  $x$  for  $Q^2 = 18 \text{ GeV}^2$  (filled circles) compared to various H1 and ZEUS separate measurements.

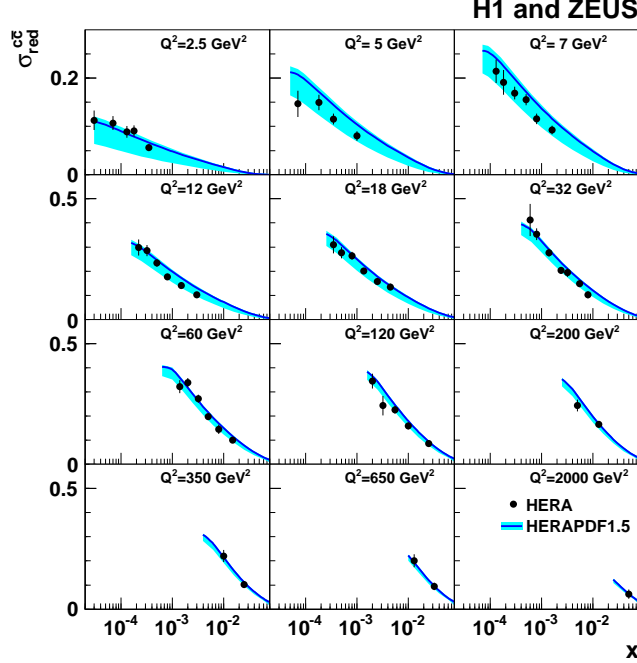


**Figure 12.** Combined reduced cross sections  $\sigma_{red}^{cc}$  as a function of  $x$  for fixed values of  $Q^2$  (filled circles) compared to NLO GM-VFNS predictions in the RT standard scheme. Lines are predictions with  $M_c = 1.4$  GeV. The bands show the full PDF uncertainty which is dominated by the  $M_c$  variation.

$1.2 < M_c < 1.8$  GeV in steps of 0.1 GeV. All cross sections rise monotonically with  $M_c$ . For any fixed  $M_c$  there is a significant spread of about 6% between the various predictions. This uncertainty is reduced to  $\approx 1.4 - 2$  % when taking  $M_c^{opt}$  for each scheme.

In Figure 17 the combined charm reduced cross sections as a function of  $x$  for fixed values of  $Q^2$  are compared to the prediction of the ABM group in FFNS at NLO and NNLO. This prediction uses the running-mass definition in the  $\overline{MS}$  scheme instead of the pole mass scheme. The data are well described in the full kinematic region with similar predictions of NLO and NNLO, indicating less sensitivity to higher order corrections.

In Figure 18 the  $\chi^2$  values of the PDF ABM fit to the combined HERA DIS data, including the charm measurements, are shown as a function of the running charm quark mass  $m_c(m_c)$ , defined in the  $\overline{MS}$  scheme. The same minimisation procedure is used here as was done for the VFNS fit. The fit of a parabolic function results in a value of  $m_c(m_c) = 1.26 \pm 0.05_{exp.} \pm 0.03_{mod.} \pm 0.02_{param.} \pm 0.02_{\alpha_s}$  GeV. The uncertainties are, respectively, experimental, model, parameterisation and  $\alpha_s$ . This measurement is consistent with the PDG value of  $1.275 \pm 0.025$  GeV.

The running charm quark mass  $m_c(m_c)$  was extracted separately for 6 different kinematic ranges in  $\mu = \sqrt{\langle Q^2 \rangle + 4m_c(m_c)^2}$ , where  $\langle Q^2 \rangle$  is the logarithmic average  $Q^2$  of the subset. In Figure 19  $m_c(m_c)$  is plotted as a function of  $\mu$ . The red point at the scale  $m_c$  and the band are the PDG average value and its error.  $m_c(m_c)$  can be translated to  $m_c(\mu)$  by  $m_c(\mu) = m_c(m_c) \frac{(\frac{\alpha_s(\mu)}{\pi})^{\beta_0 - 1}}{(\frac{\alpha_s(m_c)}{\pi})^{\beta_0 - 1}}$ , where  $\beta_0 = 9/4$  for 3 flavours. In Figure 20  $m_c(\mu)$  is plotted as

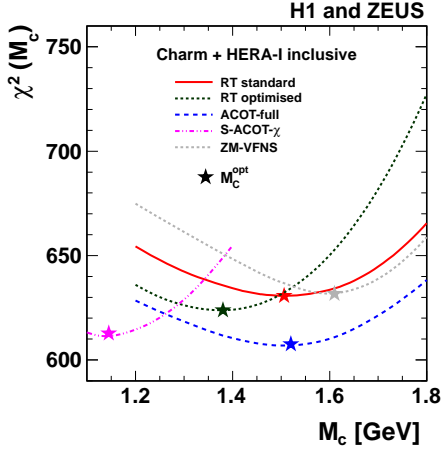


**Figure 13.** The  $\chi^2(M_c)$  values for the fit to the combined HERA inclusive DIS and charm measurements. The different HFL schemes are presented by lines. The minimal  $\chi^2$  values for each scheme at  $M_c = M_c^{opt}$  are indicated by stars.

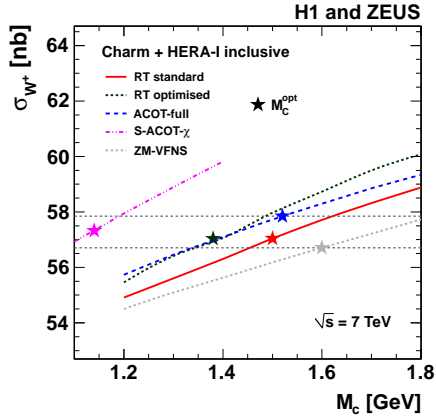


**Figure 15.** NLO predictions from the PDF fits for  $W^+$  production cross section at the LHC for  $\sqrt{s} = 7$  TeV calculated for each scheme for  $1.2 < M_c < 1.8$  GeV in 0.1 GeV steps. The predictions with  $M_c^{opt}$  values are indicated by stars. Horizontal lines show the spread of the predictions when choosing  $M_c = M_c^{opt}$ .

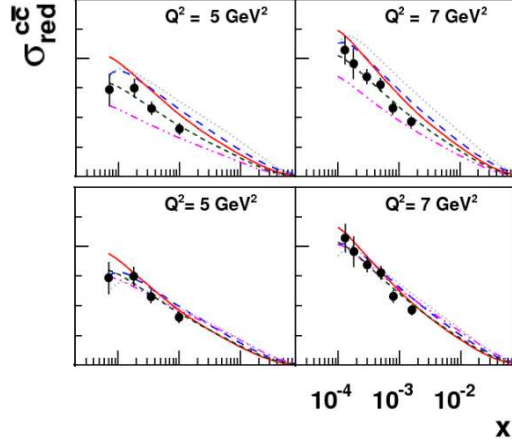


**Figure 14.** Combined reduced cross sections  $\sigma_{red}^{c\bar{c}}$  as a function of  $x$  for  $Q^2$  values of 5 and 7 GeV<sup>2</sup> (filled circles) compared to fit results using different VFNS schemes (lines). Upper plots are for  $M_c = 1.4$  GeV and lower plots are for  $M_c = M_c^{opt}$ .

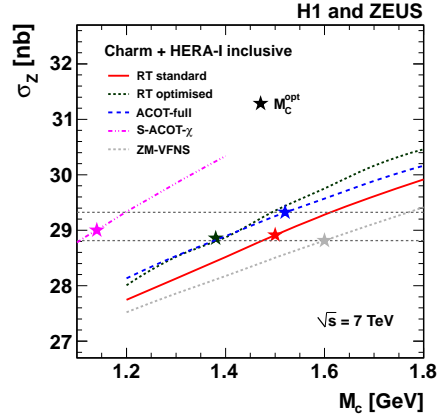


**Figure 16.** Same as Figure 15 for  $Z^0$  production at the LHC.

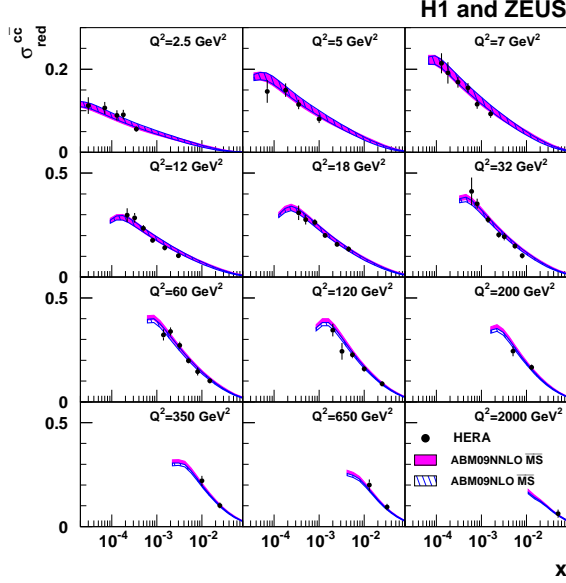


**Figure 17.** Combined reduced cross sections  $\sigma_{red}^{cc}$  as a function of  $x$  for fixed values of  $Q^2$  (filled circles). The data are compared to the ABM predictions at NLO and NNLO (shaded band) in FFNS using the  $\overline{MS}$  definition for the charm quark mass.

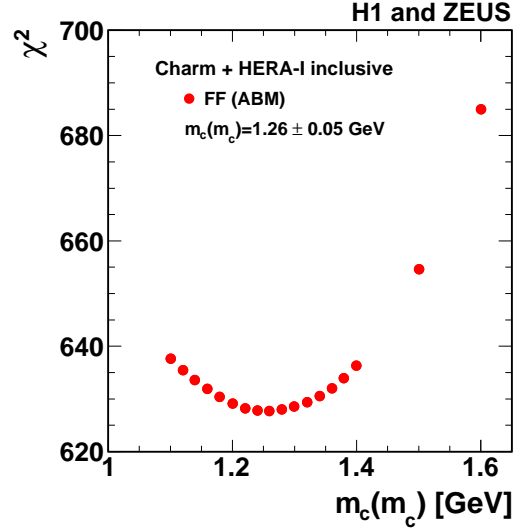


**Figure 18.**  $\chi^2$  values of the PDF fit to the combined HERA DIS data including charm measurements as a function of the running charm quark mass  $m_c(m_c)$  with the FFNS ABM scheme. The charm quark mass is defined in the  $\overline{MS}$  scheme.

a function of  $\mu$ . The red point and the band are the PDG value with the evolved uncertainty. The data are consistent with the expected QCD running of  $m_c$ . This is the first measurement of  $m_c(\mu)$  from the combined HERA charm reduced cross section data, and is an important consistency check for the running  $m_c$ , analogous to the running  $m_b$  measured at LEP.

## 7. Combination of $D^{*\pm}$ differential cross sections in DIS

Differential cross sections for inclusive  $D^{*\pm}$ -meson production in DIS from H1 and ZEUS measurements have been combined in a common visible phase-space region of  $Q^2 > 5 \text{ GeV}^2$ ,  $0.02 < y < 0.7$ ,  $p_T(D^*) > 1.5 \text{ GeV}$  and  $|\eta(D^*)| < 1.5$  [5]. The correlations in the systematic uncertainties were fully taken into account.

In Figs.21-22 the differential cross sections are plotted, respectively, as a function of  $p_T(D^*)$  and  $|\eta(D^*)|$ . There is an impressive reduction of the uncertainties in the combined results compared to the individual H1 and ZEUS measurements. The precision of the combined data is about 5% in a large fraction of the phase space. Similar results and precision is also obtained for the differential cross sections as a function of  $Q^2$  and  $y$ .

In Figs.23-26 the combined  $D^*$  differential cross sections as a function of  $p_T(D^*)$ ,  $|\eta(D^*)|$ ,  $Q^2$  and  $y$  are compared to the NLO FFNS HVQDIS program. Since the data points are given in a limited kinematic region without extrapolation to the full phase-space, the theoretical uncertainties in the data points are negligible, yielding a combined data precision of about 5% over a large fraction of the measured phase-space. The NLO predictions describe the data within large uncertainties of  $\approx 10 - 30\%$ .

The HVQDIS setup for the process  $ep \rightarrow c\bar{c}X \rightarrow D^*X$  uses some arbitrary variable

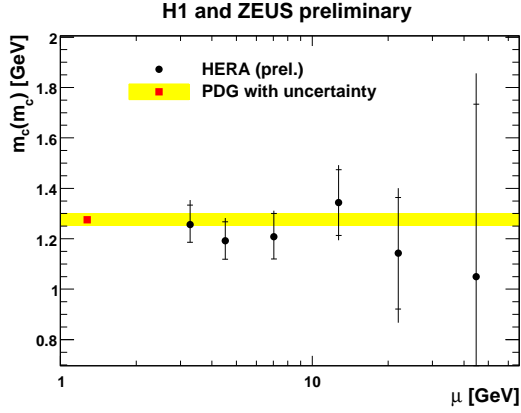


**Figure 19.**  $m_c(m_c)$  as a function of  $\mu = \sqrt{\langle Q^2 \rangle + 4m_c(m_c)^2}$ . The red point at the scale  $m_c$  and the band are the PDG average value and its error.

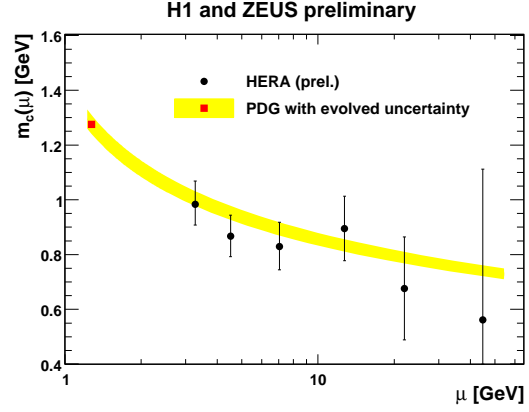


**Figure 20.**  $m_c(\mu)$  as a function of  $\mu$ . The red point and the band are the PDG value with the evolved uncertainty.

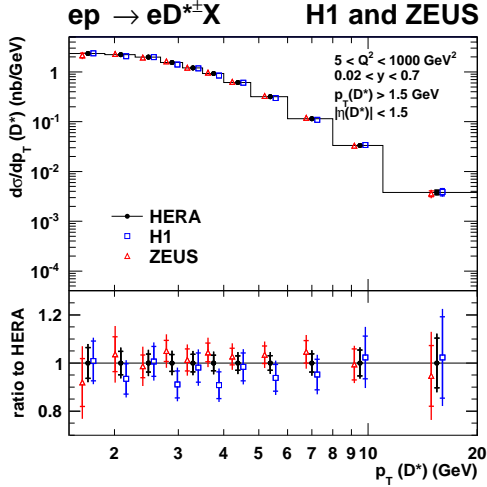


**Figure 21.** Differential  $D^{*\pm}$  cross section as a function of  $p_T(D^*)$ . Filled points are combined cross sections. The bottom part shows the ratio of the cross sections to the central value of the combined cross sections.

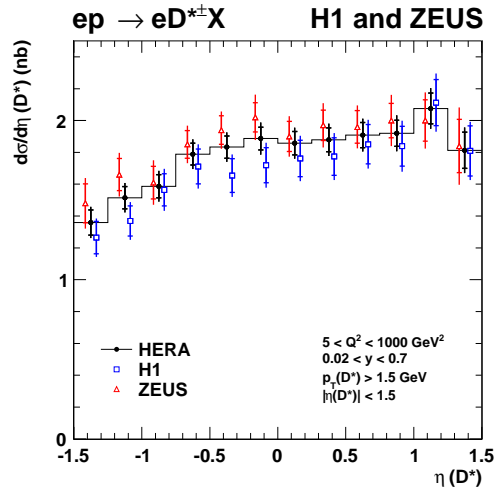


**Figure 22.** Differential  $D^{*\pm}$  cross section as a function of  $|\eta(D^*)|$ . Filled points are combined cross sections.

definitions, e.g.  $\mu_r = \mu_f = \sqrt{Q^2 + 4m_c^2}$ ,  $m_c^{pole} = 1.5$  GeV, where  $\mu_r$  and  $\mu_f$  are, respectively, the renormalisation and factorisation scales. In order to improve the agreement with the data, some parameters in the HVQDIS setup were changed such that the normalisation and shapes of all differential cross sections will describe the data well. Such an agreement was found with  $\mu_r = 0.5\sqrt{Q^2 + 4m_c^2}$ ,  $m_c^{pole} = 1.4$  GeV and with some softening of the fragmentation function used for the calculation. All other parameters were left at their default values. The HVQDIS results with these parameters (“NLO QCD customised”) are also shown in Figs.23-26 as red

histograms. As expected, the NLO customised histograms describe the data very well. It should be emphasized that this is not a prediction, but it may hint at which direction the theory can be improved. NNLO calculations and improved fragmentation models may replace the “customised” treatment.

Similar conclusions are obtained for  $D^*$  double-differential cross sections in  $Q^2$  and  $y$ .

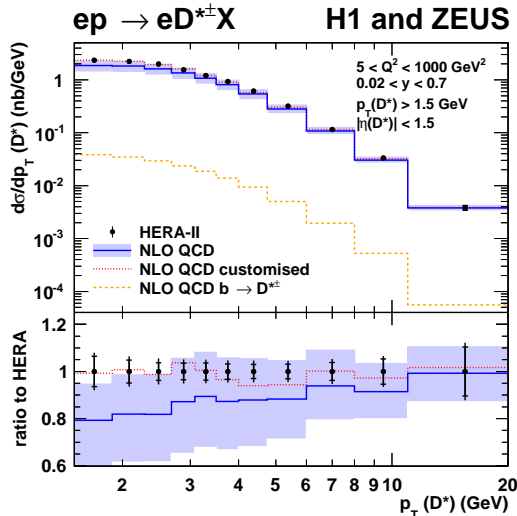


**Figure 23.** Differential  $D^*$  cross section as a function of  $p_T(D^*)$ . The data points are the combined cross sections. Also shown are the NLO predictions from HVQDIS and their uncertainty band. The customised NLO calculation is shown as the red histogram. The bottom part shows the ratio of these cross sections to the central value of the combined cross sections.

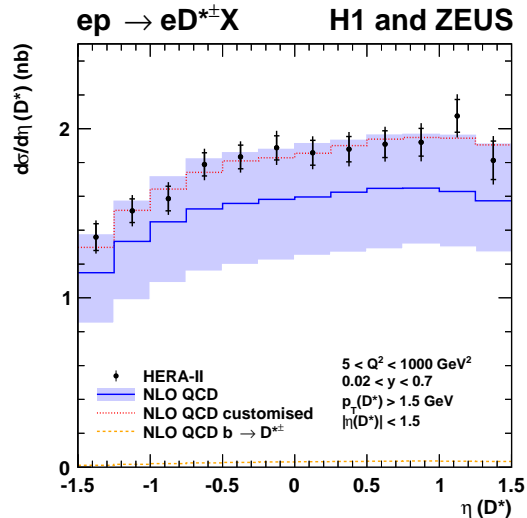


**Figure 24.** Differential  $D^*$  cross section as a function of  $|\eta(D^*)|$ . The data points are the combined cross sections. Also shown are the NLO predictions from HVQDIS and their uncertainty band. The customised NLO calculation is shown as the red histogram.

## 8. Beauty production in DIS

Beauty cross sections at HERA are much smaller than the charm ones. The production of  $b$  quarks has been studied with the ZEUS detector for  $5 < Q^2 < 1000 \text{ GeV}^2$  [6]. The beauty content in events with at least one jet has been extracted using the invariant mass of charged tracks associated with secondary vertices,  $m_{vtx}$ , and the decay-length significance of these vertices,  $S$ , defined as  $d/\delta d$ , where  $d$  is the vector in  $X - Y$  between the secondary vertex and the interaction point projected onto the jet axis in the  $X - Y$  plane and  $\delta d$  is its uncertainty. The invariant mass  $m_{vtx}$  provides a distinguishing variable for jets from  $b$  and  $c$  quarks, reflecting the different masses of the  $b$  and  $c$  hadrons.

Control distributions of  $E_T^{jet}$ ,  $\eta^{jet}$ ,  $Q^2$  and  $x$  are shown in Figure 27 after  $b$  enrichment cuts ( $2 < m_{vtx} < 6 \text{ GeV}$  and  $|S| > 8$ ) for  $E_T^{jet} > 5.0 \text{ GeV}$ . All data distributions are well described by the Monte Carlo (MC).

Differential cross sections for inclusive jet production in enriched  $b$  events as a function of  $Q^2$  and  $x$  are shown in Figs.28-29. The measurements are compared to the HVQDIS NLO FFNS

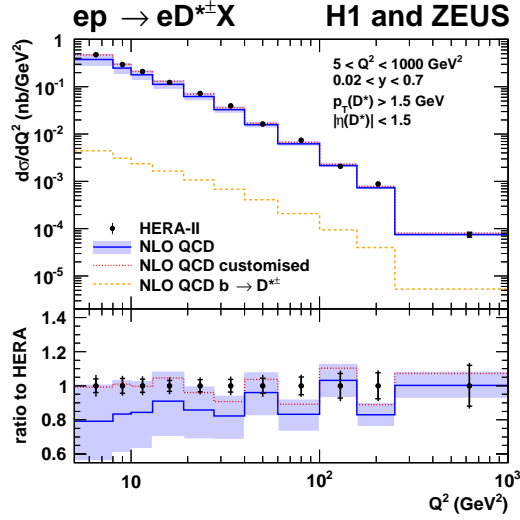


**Figure 25.** Differential  $D^*$  cross section as a function of  $Q^2$ . The data points are the combined cross sections. Also shown are the NLO predictions from HVQDIS and their uncertainty band. The customised NLO calculation is shown as the red histogram. The bottom part shows the ratio of these cross sections to the central value of the combined cross sections.

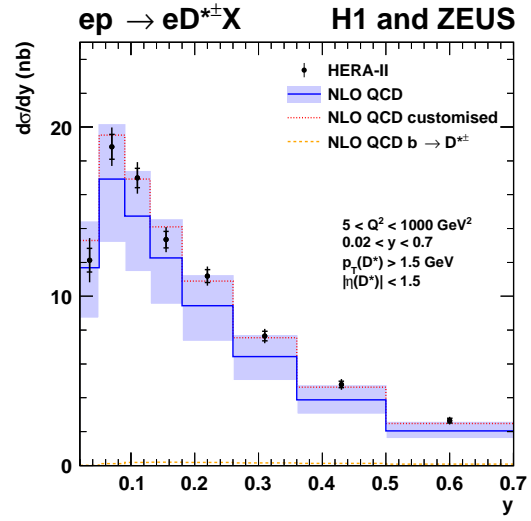


**Figure 26.** Differential  $D^*$  cross section as a function of  $y$ . The data points are the combined cross sections. Also shown are the NLO predictions from HVQDIS and their uncertainty band. The customised NLO calculation is shown as the red histogram.

predictions. The cross sections are reasonably well described by the predictions.

The structure function  $F_2^{bb}$  as a function of  $Q^2$  for fixed  $x$  values (filled circles) is compared in Figure 30 to previous ZEUS and H1 measurements and to predictions of FFNS and GM-VFNS NLO and NNLO predictions. This measurement represents the most precise determination of  $F_2^{bb}$  in a wide range of  $Q^2$  at HERA. All predictions provide a reasonable description of the data.

The reduced beauty cross section,  $\sigma_{red}^{bb}$ , as a function of  $x$  for fixed  $Q^2$  values is shown in Figure 31. It was used, together with inclusive DIS data, to determine the  $b$ -quark mass in a QCD fit as was done for the  $c$ -quark mass. Lines are the fit results with  $m_b = 4.07$  (best fit), 3.93 and 4.21 GeV. The sensitivity to  $m_b$  comes mostly from the low  $Q^2$  values.

In Figure 32 the  $\chi^2$  values of the PDF fit to the DIS data, including the beauty measurements, are shown as a function of the running  $b$ -quark mass  $m_b(m_b)$ , defined in the  $\overline{MS}$  scheme. The same minimisation procedure is used here as was done for the charm fit. A clear dependence on  $m_b$  is seen. The  $b$ -quark mass and its uncertainty are determined from a parabolic parameterisation, yielding:  $m_b(m_b) = 4.07 \pm 0.14$  (fit) $_{-0.07}^{+0.01}$  (mod.) $_{-0.00}^{+0.05}$  (param.) $_{-0.05}^{+0.08}$  (theo.) GeV. The uncertainties come, respectively, from the fit, model, parameterisation and theory. This measurement is consistent with the PDG value of  $4.18 \pm 0.03$  GeV, which was derived from lattice QCD and time-like processes.

As was done for  $m_c(m_c)$ ,  $m_b(m_b)$  can be translated to  $m_b(\mu)$  with  $\mu = 2m_b$ . Figure 33 shows  $m_b(\mu)$  as a function of  $\mu$  of this measurement compared to PDG and to LEP results. The running of the  $b$ -quark mass is consistent with QCD.

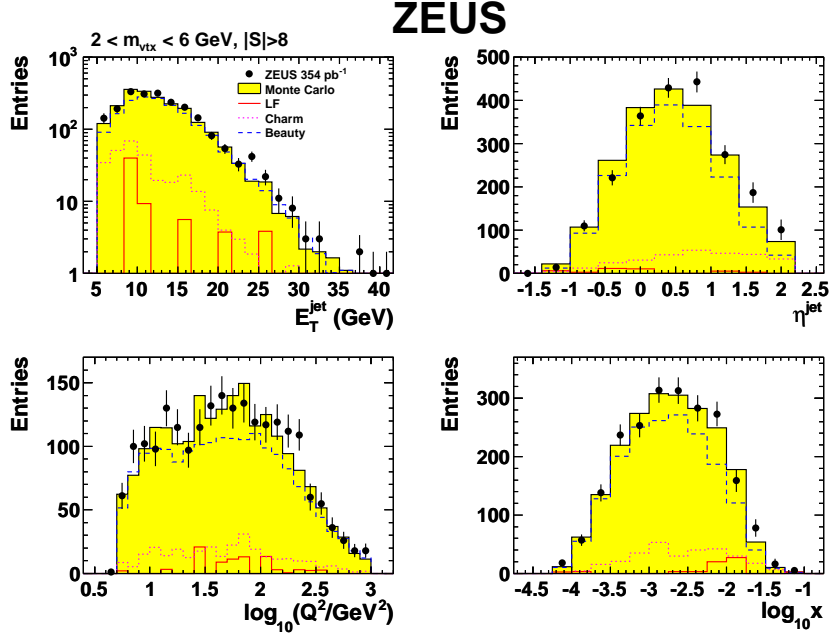


**Figure 27.** Distributions of  $E_T^{jet}$ ,  $\eta^{jet}$ ,  $Q^2$  and  $x$  of the selected secondary vertices for a  $b$ -enriched subsample with  $2 < m_{vtx} < 6$  GeV and  $|S| > 8$ . The data are compared to the MC contributions from the  $b$ ,  $c$  and light-flavour subsamples and to their sum.

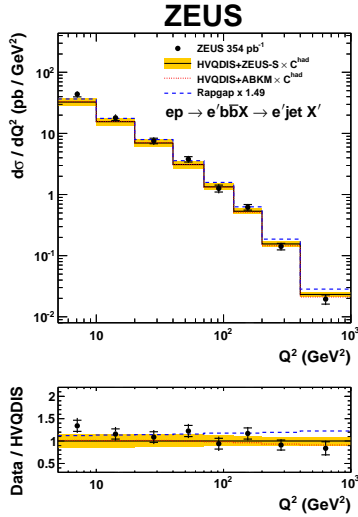


**Figure 28.** Differential cross sections for inclusive jet production in enriched  $b$  events as a function of  $Q^2$ . The full lines are HVQDIS predictions with uncertainties indicated by the band. The dashed lines are RAPGAP MC predictions.

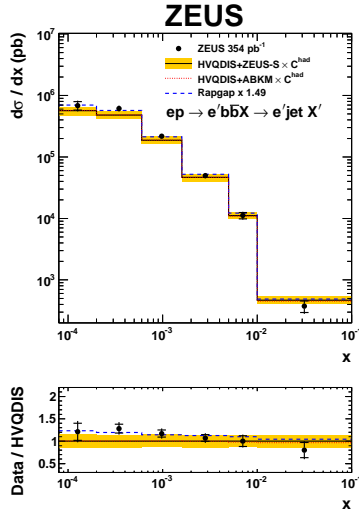


**Figure 29.** Differential cross sections for inclusive jet production in enriched  $b$  events as a function of  $x$ . The lines are as in Figure 28.

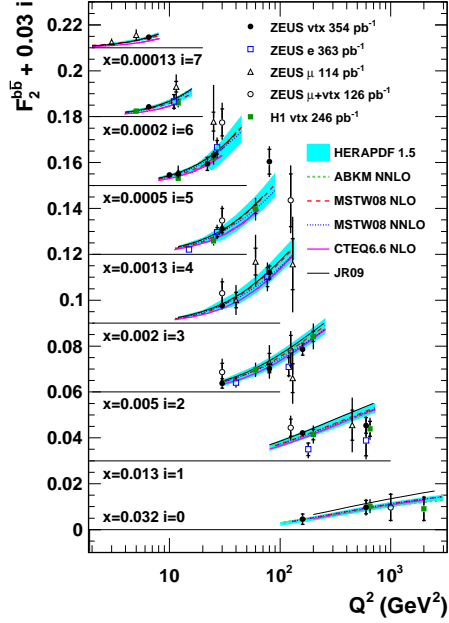


**Figure 30.** The structure function  $F_2^{bb}$  (filled circles) as a function of  $Q^2$  for fixed  $x$  values compared to previous H1 and ZEUS results and to several NLO and NNLO QCD calculations.

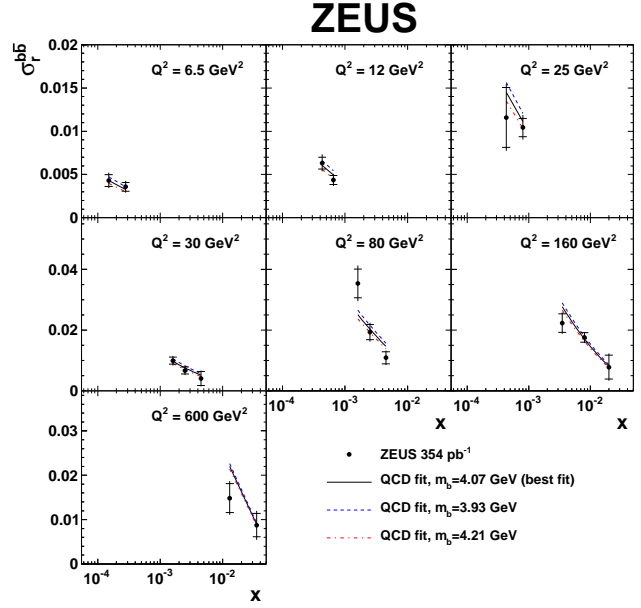


**Figure 31.** Reduced  $b$  cross section  $\sigma_{red}^{bb}$  (filled circles) as a function of  $x$  for different  $Q^2$  values. Also shown are results of a QCD fit. Central line is the best fit. Lower and upper lines are, respectively, fits for a higher and a lower  $b$  mass.

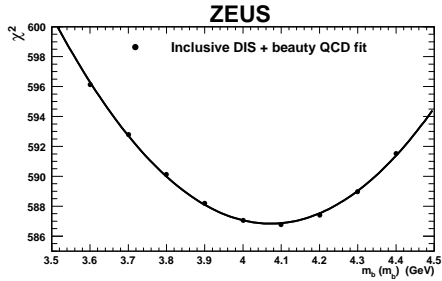


**Figure 32.** The  $\chi^2$  values for the PDF fit to the combined HERA DIS data, including the  $b$  measurements, as a function of the running  $b$  quark mass  $m_b(m_b)$ . The FFNS ABM scheme is used, where the  $b$  quark mass is defined in the  $\overline{MS}$  scheme. The solid line is a second order polynomial parameterisation of the points.

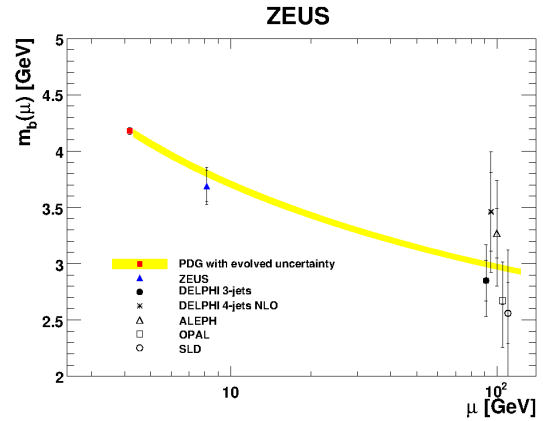


**Figure 33.**  $m_b(m_b)$  as a function of  $\mu = 2m_b$ . The red point and the yellow band are the PDG value with its evolved uncertainty. The points at the high  $\mu$  range are various LEP results.

## 9. Summary

- The H1 and ZEUS Collaborations are still providing new charm(ing) and beauty(full) results with the full HERA data. These results yield tighter constraints on QCD.
- The cross section of  $D^{*\pm}$  production in photoproduction as a function of the  $ep$  CM energy was measured for the first time at HERA. The  $D^*$  cross sections increase with  $\sqrt{s}$  as predicted by NLO QCD.
- New precise charm fragmentation fractions measurements in photoproduction are competitive with  $e^+e^-$  collisions and support charm fragmentation universality.
- New DIS charm measurements and HERA charm data combination provide constraints on PDFs and on QCD heavy quark calculations.
- Most of the HERA DIS charm data of H1 and ZEUS were combined:
  - Consistent data sets have been extracted using different methods yielding reduced uncertainties.
  - The data are well described by FFNS and GM-VFNS QCD predictions.
  - The choice of optimal  $M_c$  parameters for different VFNS schemes improves the predictions of  $W, Z$  cross sections at the LHC.
  - The running charm mass in the  $\overline{MS}$  FFNS scheme was measured, yielding  $m_c(m_c) = 1.26 \pm 0.06$  GeV in agreement with PDG. This is the first measurement of the charm-mass running at HERA.
- The visible  $D^{*\pm}$  cross sections of H1 and ZEUS were combined. Since no extrapolation to the full kinematic region was performed, theory uncertainties in the data are negligible. The results challenge theory and fragmentation models.
- New precise  $b$ -jet measurements with a lifetime tag in DIS events have been performed using secondary vertices. The  $b$ -mass was measured in the  $\overline{MS}$  scheme yielding  $m_b(m_b) = 4.07 \pm 0.17$  GeV in agreement with the PDG value. The data are well described by NLO QCD predictions and the  $b$ -mass running is consistent with QCD.

## References

- [1] ZEUS Collaboration, H.Abramowicz et al., JHEP10(2014)003.
- [2] ZEUS Collaboration, H.Abramowicz et al., JHEP09(2013)058.
- [3] ZEUS Collaboration, H.Abramowicz et al., JHEP05(2013)023.
- [4] H1 and ZEUS Collaborations, F.D.Aaron et al., EPJ C73(2013)2311.
- [5] H1 and ZEUS Collaborations, H.Abramowicz et al., hep-ex:1503.06042, to be published in JHEP.
- [6] ZEUS Collaboration, H.Abramowicz et al., JHEP09(2014)127.